Nuclear Physics A549 (1992) 387–406
North-Holland

NUCLEAR
PHYSICS A

Photodisintegration of the deuteron by linearly polarized photons*

K.-H. Krause[1], J. Sobolewski[1], J. Ahrens[1], J.M. Henneberg[1] and B. Ziegler
Max-Planck-Institut für Chemie, Kernphysikalische Arbeitsgruppe, D-6500 Mainz, Germany

Received 10 May 1992

Abstract: The photodisintegration of the deuteron has been studied using a quasi-monochromatic linearly polarized photon beam at the energies of 54, 60, 68 and 88 MeV. The photon beam was obtained by tagging off-axis bremsstrahlung photons. The angular distribution of the azimuthal cross-section asymmetry and the polarization-independent part of the differential cross section were measured simultaneously at seven reaction angles between 40° and 160°. The experimental results are discussed in view of theoretical predictions.

E | NUCLEAR REACTIONS ^{2}H(polarized γ, p)n, $E = 54$, 60, 68 and 88 MeV, $\theta_p = 40°$–160°; measured $\sigma(E, \theta_p)$ and polarization asymmetry. Model comparison. Quasi-monochromatic linearly polarized photon beam, liquid target, semiconductor detectors.

1. Introduction

The photodisintegration of the deuteron is a basic nuclear process. This two-body breakup is important for studies of the electromagnetic properties of the nucleons and the elementary nucleon–nucleon interaction. Since the pure electromagnetic interaction in photon absorption is well understood and sufficiently weak in order to allow a lowest-order perturbative approach, the comparison between experiment and theory directly tests the theoretical description of the deuteron.

Accompanied by the development of realistic nucleon–nucleon potentials, extensive studies of the photodisintegration of the deuteron have been carried out in the framework of conventional non-relativistic nuclear physics. At first only nucleon degrees of freedom and no exchange effects (except those included implicitly in the Siegert operators) were considered. Refined calculations of this process at photon energies below pion-production threshold indicate the importance of explicit meson-exchange currents and virtual excited isobar configurations as well as relativistic corrections to the nuclear charge density [a recent review can be found in ref. [1])].

Correspondence to: Dr. K.-H. Krause, Institute of Nuclear Physics, University of Mainz, J.-J. Becher-Weg 45, D-6500 Mainz 1, Germany.

* This work was supported by the Deutsche Forschungsgemeinschaft, SFB201.

[1] Present address: Institut für Kernphysik, J. Gutenberg-Universität, D-6500 Mainz, Germany.

Significant contributions from these effects can be expected in the angular distribution of the polarization-independent part of the differential cross section and in the azimuthal cross-section asymmetry for a linearly polarized photon beam.

From the experimental point of view these observables have not been adequately studied even at medium energies below pion-production threshold. In this energy range large discrepancies exist among the angular distributions of the absolute cross section, which were all obtained using continuous bremsstrahlung [2-6]). For the azimuthal cross-section asymmetry the situation is similar. There the measurements can be impaired by an insufficient knowledge of the degree of linear polarization of the photon beam. There are little data available [7-12]), and some of that are contradictory.

The excellent properties of the electron beam from the continuous-wave accelerator MAMI (Mainz Microtron) at the Institut für Kernphysik of the University of Mainz [13]) make possible a new generation of precision experiments. In combination with the bremsstrahlung tagging system of the Max-Planck-Institut für Chemie in Mainz [14]) this potential can be utilized for the investigation of photonuclear processes.

The aim of the work described here was to perform new cross-section measurements for the photodisintegration of the deuteron in the energy range from 50 to 90 MeV using a quasi-monochromatic and linearly polarized photon beam.

The differential cross section for the reaction ^{2}H(γ, p)n can be written as [15])

$$\frac{d\sigma}{d\Omega}(\theta_p^{c.m.}, \phi) = \frac{d\sigma_0}{d\Omega}(\theta_p^{c.m.}) + P\frac{d\sigma_1}{d\Omega}(\theta_p^{c.m.}) \cos 2\phi, \tag{1}$$

where $\theta_p^{c.m.}$ is the angle between the photon and the proton momenta in the center-of-mass system, ϕ the angle between the reaction plane and the polarization plane and P the degree of linear polarization of the photon beam. For unpolarized incident photons the differential cross section is given by $d\sigma_0/d\Omega$. A linearly polarized photon beam leads to an azimuthal asymmetry in the differential cross section due to the quantity $d\sigma_1/d\Omega$. With the definition of the azimuthal cross-section asymmetry,

$$\Sigma(\theta_p^{c.m.}) = \frac{d\sigma_1/d\Omega}{d\sigma_0/d\Omega}, \tag{2}$$

the expression for the differential cross section becomes

$$\frac{d\sigma}{d\Omega}(\theta_p^{c.m.}, \phi) = \frac{d\sigma_0}{d\Omega}(\theta_p^{c.m.})[1 + P\Sigma(\theta_p^{c.m.}) \cos 2\phi]. \tag{3}$$

The polarization-independent part of the differential cross section and the azimuthal cross-section asymmetry can be obtained by measuring the differential cross section parallel ($\parallel$) and perpendicular ($\perp$) to the polarization plane. The

polarization-independent part of the differential cross section follows from

$$\frac{d\sigma_0}{d\Omega}(\theta_p^{c.m.}) = \frac{1}{2}\left(\frac{d\sigma_\parallel}{d\Omega} + \frac{d\sigma_\perp}{d\Omega}\right). \tag{4}$$

The determination of the azimuthal cross-section asymmetry,

$$\Sigma(\theta_p^{c.m.}) = \frac{1}{P}\,\frac{d\sigma_\parallel/d\Omega - d\sigma_\perp/d\Omega}{d\sigma_\parallel/d\Omega + d\sigma_\perp/d\Omega}, \tag{5}$$

in addition requires the knowledge of the degree of linear polarization P of the photon beam. The photon flux and the number of target atoms per cm^2 can be eliminated from the determination of the asymmetry - as was done in this work - by simultaneously detecting the photo-protons at $\phi = 0°$ and 90°.

2. Experiment

Two essentially independent setups are combined in the experiment described here. They are a bremsstrahlung tagging system and the reaction chamber, which contains the liquid-deuterium target and the photo-proton detection system. The setup is shown schematically in fig. 1. The properties of the tagging system including

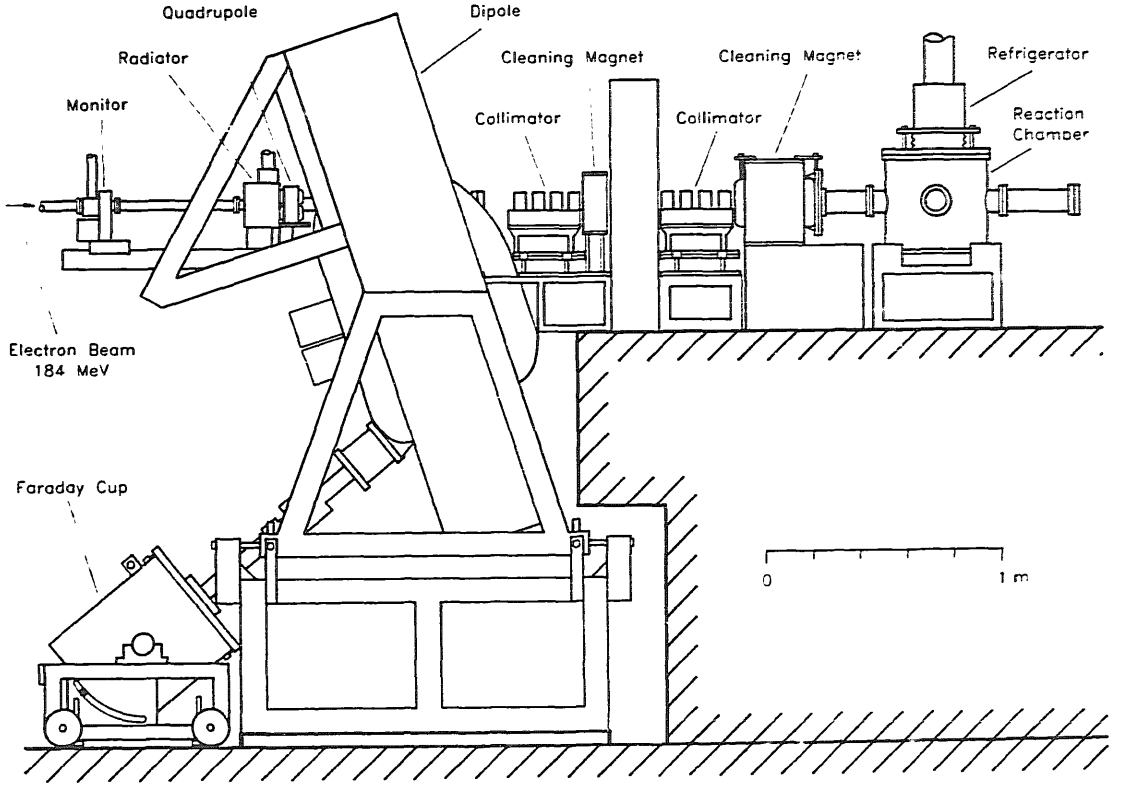

Fig. 1. Side view of the experimental setup: the bremsstrahlung tagging spectrometer, the photon collimation with the cleaning system and the reaction chamber, which contains the liquid-deuterium target and the photo-proton detection system.

its data acquisition system are described in detail elsewhere [14]) - only an outline is given here.

2.1. PHOTON SOURCE

The source of the quasi-monochromatic linearly polarized photon beam is the bremsstrahlung tagging system of the Max-Planck-Institut für Chemie in Mainz [14]) installed at the electron beam from MAMI A (see fig. 1). The overall design of the tagging spectrometer may be considered as standard, but the magnetic electron optics were chosen in such a way, that the degree of linear polarization of a tagged off-axis collimated photon beam can be enhanced considerably.

The tagging spectrometer consisting of a quadrupole and dipole magnet has a large angular acceptance of more than five characteristic post-bremsstrahlung electron angles and a large-momentum acceptance, p_{max}/p_{min}, of more than 4/1. The slightly curved chromatic image line is located inside the magnetic field of the dipole. At the primary electron energy of 184 MeV, photons with energies E_γ from 14 to 144 MeV can simultaneously be tagged.

The linear polarization of an off-axis photon beam can be enhanced by means of a kinematic selection of the post-bremsstrahlung electrons, i.e. those electrons whose associated bremsstrahlung photons do not have the desired polarization must preferentially be rejected from tagging. This is possible as the direction of the electric-field vector of the bremsstrahlung photon is correlated with the angular change of the electron in the bremsstrahlung process. In the non-bend plane of the spectrometer the displacement of the electron is proportional to its angular change in the bremsstrahlung process and to a good approximation independent of its displacement at the radiator. Thus the post-bremsstrahlung electrons can be "collimated" by selecting the position and size of the tagging detectors.

The tagging detector system is based on silicon surface barrier detectors (Si(sb), Micron Semiconductor MSX5-450-C) with a sensitive area of $5 \times 5\,mm^2$ and a depletion-layer depth of 450 μm. This type of detector makes it possible to achieve a precise collimation of the electrons. The Si(sb) detectors are grouped in two separate arrays. Each array contains 16 detectors mounted in two adjacent parallel rows, which are sited symmetrically around the median line of the image plane (an accuracy of 0.1 mm has been found to be sufficient). Tagged photons from 53 to 71 MeV and 84 to 104 MeV are simultaneously provided. The detector width corresponds to an energy resolution of approximately 1 MeV. An important feature of the detector arrangement is its suitability for precise monitoring of the electron-beam alignment in the non-bend plane - a properly aligned beam results in the same count rates for each symmetric pair of detectors.

A numerical integration of the bremsstrahlung differential cross section was performed in order to find the geometry for the electron and photon collimation that gives optimal values for the essential parameters of the tagging system, i.e. the

figure of merit $\varepsilon_t P^2$ has to be maximized, where ε_t is the tagging efficiency and P the degree of linear polarization of the tagged photon beam. In the photon-energy range from 50 to 100 MeV the tagging efficiency for the optimized geometry increases monotonically from 22% to 36%, whereas the corresponding degree of linear polarization decreases from 47% to 35%. Due to the kinematic selection of the post-bremsstrahlung electrons the figure of merit is enhanced by a factor of six.

Uncertainties in the geometry of the electron and photon collimation led to a relative uncertainty in the prediction of the degree of linear polarization of less than 2%. Multiple scattering in the radiator broadens the angular distribution of the post-bremsstrahlung electrons as well as the distribution of the photons. In order to preserve the polarization of the elementary bremsstrahlung process an aluminium foil with a thickness of 6 μm (6.4×10^{-5} radiation length) was used as radiator, thereby keeping the relative degradation of the degree of polarization due to multiple scattering less than 0.3%.

A measurement of the degree of linear polarization has been performed using the radiation characteristics of photons emitted from resonance excitation of the prominent 15.11 MeV (1^+) level of ^{12}C. The experimental values obtained at different electron collimations agree with the bremsstrahlung calculation. In contrast to the degree of linear polarization the tagging efficiency can easily be measured with high precision (see table 1). For this purpose a NaI spectrometer was placed directly in the collimated photon beam and operated in coincidence with the tagging detectors. The measured tagging efficiencies are also in agreement with the prediction.

Since a maximum count rate of 1.3 MHz per Si(sb) detector was achieved the total flux of the quasi-monochromatic linearly polarized photon beam was $4\times10^6\ s^{-1}$.

2.2. LIQUID-DEUTERIUM TARGET

Along the beam direction the cryotarget consists of three successive cells separated by 2 μm Mylar foils. The two outer volumes are separated from vacuum by 100 μm Kapton windows. Only the inner volume (84 mm diameter × 10 mm), the actual

TABLE 1

Calculated degree of linear polarization P and, measured in the course of the experiment described here, ε_t the tagging efficiency, N_e the number of counts observed in the tagging detectors and $N_\gamma = \varepsilon_t N_e$ the number of quasi-monochromatic photons. The data of 12 tagging detectors were combined into four groups, with the average photon energies E_γ. The given uncertainties are the statistical errors.

E_γ (MeV):	54	60	68	88
P (%)	47.3	46.6	45.2	39.3
ε_t (%)	24.35 ± 0.27	25.54 ± 0.26	27.66 ± 0.28	33.78 ± 0.32
N_e (10^{10})	41.02	50.35	50.54	54.62
N_γ (10^{10})	9.99 ± 0.11	12.86 ± 0.13	13.98 ± 0.14	18.45 ± 0.17

target cell, is filled with boiling liquid deuterium. The outer volumes are connected with the target cell by a pressure-compensation capillary. Consequently, the thin inner foils are exposed to hydrostatic pressure only. This leads to an almost constant thickness of the liquid-deuterium cell.

Taking into account the small curvature of the inner windows, the deuterium vapour in the outer volumes, and correcting for the contrary effect of gas bubbles in the boiling liquid deuterium the number of target nuclei was determined to be $N_t = 8.7 \times 10^{22}$ cm^{-2} with a systematic error of ±2.5%.

2.3. DETECTION SYSTEM

The photo-proton detection system (see fig. 2) is based on Si(sb) detectors (Micron Semiconductor MSX3-450-C) with a sensitive area of 1 × 1 cm^2 and a depletion-layer depth of 450 μm. The range of the protons expected here is bigger than the depletion depth of the detectors, thus an energy-loss signal is provided.

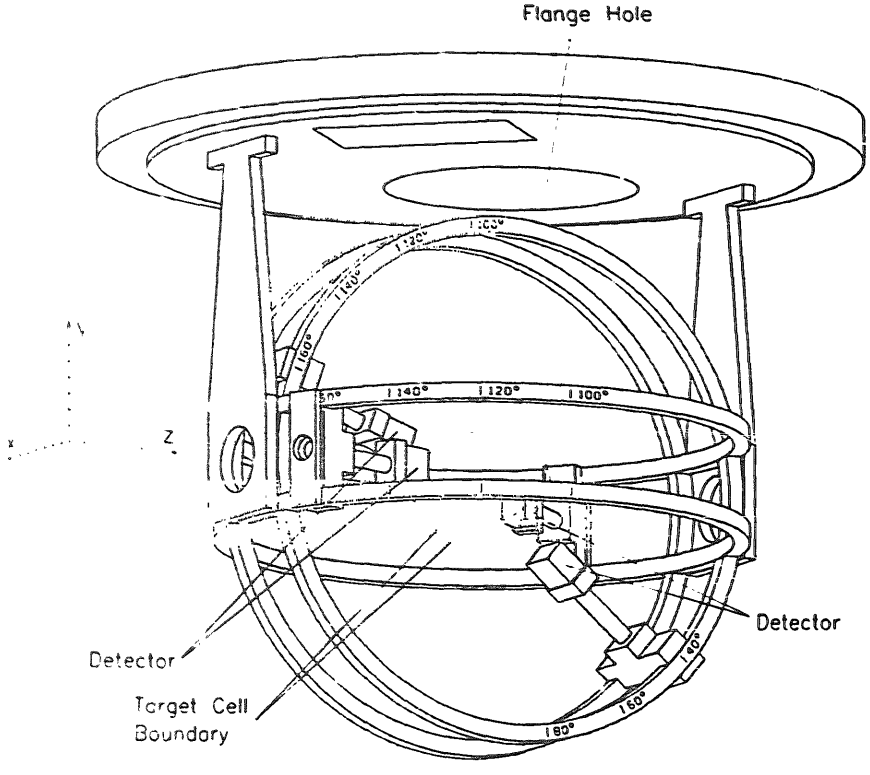

Fig. 2. The proton-detection system. The z-axis of the coordinate system corresponds to the direction of the collimated tagged-photon beam. The detectors are mounted on an arrangement of four rings (320 mm diameter) at seven reaction angles ($\theta_p = 40°$–$160°$) both parallel and perpendicular to the polarization plane, which according to ref. [14]) is the y, z plane. To simplify the figure, only the two detector pairs at the extreme angles are shown. The inclined liquid-deuterium target, the target cell of which is outlined only, is located symmetrically with regard to each pair of detectors in the center of the system.

The most important contributions to the accidental background are due to protons from photodisintegration by untagged low-energy photons, and electrons from electromagnetic processes like Compton scattering and pair production. As the energy of a photo-proton is determined by the tagged-photon energy and the reaction kinematics the energy-loss information can be utilized for background suppression.

The detectors are arranged at seven reaction angles θ_p between 40° and 160° in the laboratory system, both parallel and perpendicular to the polarization plane. With regard to the target center each of the detectors covers a solid angle of about 28 msr corresponding to $\Delta\theta_p = \pm 5°$. The liquid-deuterium target is mounted symmetrically to both reaction planes. A small azimuthal asymmetry Σ_{app}, for which the measured cross-section asymmetry has to be corrected, arises from the asymmetric intensity distribution of the off-axis photon beam, which enters the effective solid angles $\Delta\Omega$ of the detectors. The computed values for $\Sigma_{app}(E_\gamma, \theta_p) = (\Delta\Omega_\parallel - \Delta\Omega_\perp)/(\Delta\Omega_\parallel + \Delta\Omega_\perp)$ amount to not more than 0.05. Moreover, the systematic error for the azimuthal asymmetry of the apparatus due to uncertainties in the alignment of the assembly was estimated to be $\Delta\Sigma_{app} = \pm 0.007$ only.

The electronic setup, explained in detail in ref. [14]), fulfills the requirements of an event-by-event measurement. For each coincident event the following data were recorded:

- Index of the proton detector (θ_p, ϕ).
- Energy loss deposited in the proton detector (ΔE_p).
- Index of the coincident electron detector(s) (E_γ).
- Time difference between the proton and electron signals (Δt).

At the average coincidence rate of about 90 Hz a system dead time of (10.5 ± 0.2)% was determined. The experiment used 110 h of beam time.

3. Analysis

The first step in the off-line data processing was the reconstruction of the raw time-difference spectra for each set of E_γ, θ_p and ϕ. Since all events are taken into account regardless of the energy loss ΔE_p, the coincidence peaks are small compared to the background.

With appropriate software cuts in the raw time spectra we obtained two energy-loss spectra for each parameter set, one for the true and accidental, and another one for the pure accidental events, N_C^{TA} and N_C^{A}, respectively. The difference of both spectra clearly allows one to localize the photo-proton energy loss peak (see fig. 3). The width of the energy-loss peak mainly stems from the different path lengths of the protons in the target, the angular resolution of the proton-detector arrangement and the energy spread of the quasi-monochromatic photons.

By setting a software window around the energy-loss peak refined time spectra were obtained (see fig. 4). When compared with the raw time spectra, background is suppressed by about 90%. The refined time spectra can easily be analyzed with

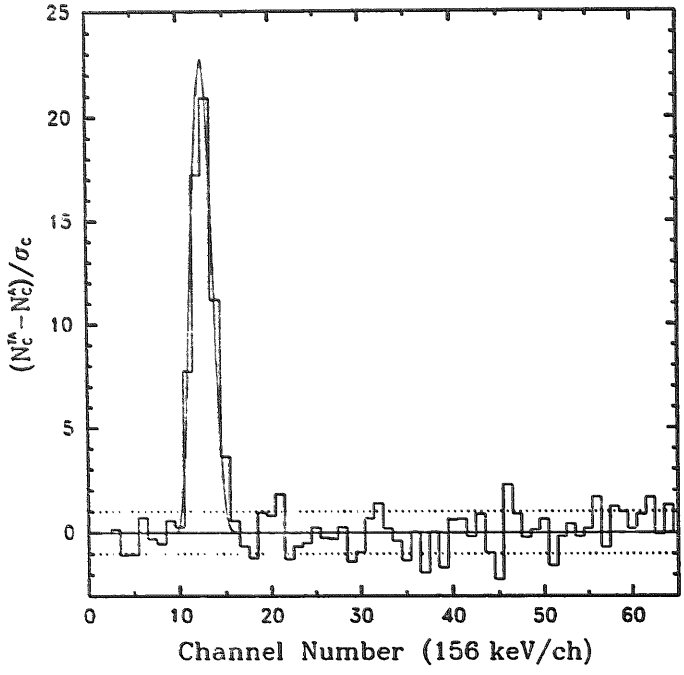

Fig. 3. Energy-loss spectrum of the photo-protons at $E_\gamma = 54$ MeV, $\theta_p = 60°$ and $\phi = 0°$. The spectrum is the difference of two pulse-height spectra: N_C^{TA} was constructed from true and accidental and N_C^A exclusively from accidental events (see text). The number of counts per channel is given in units of its statistical error, σ_C. The spectrum agrees with the calculated energy loss (solid curve).

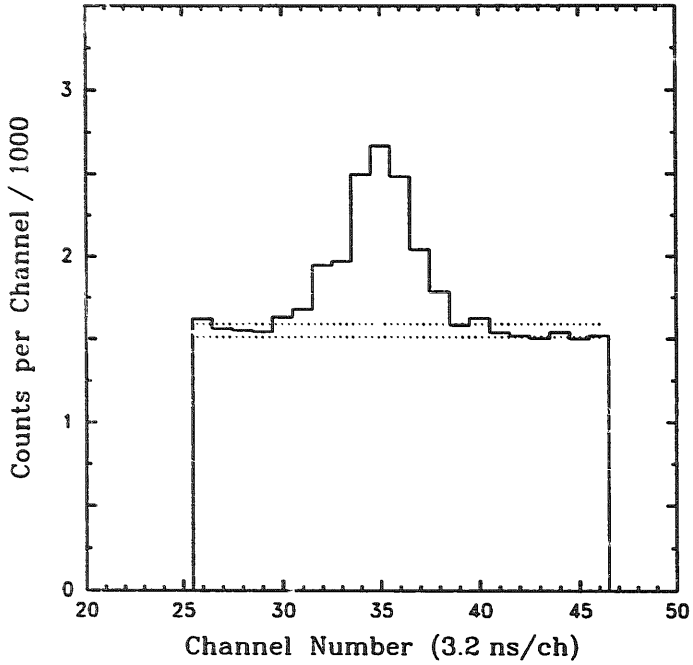

Fig. 4. Refined time-difference spectrum at $E_\gamma = 54$ MeV, $\theta_p = 60°$ and $\phi = 0°$ reconstructed with a software window around the energy-loss peak of the photo-protons shown in fig. 3. The dotted lines represent the standard deviation $\pm\sigma$ of the averaged number of accidental events per channel.

respect to the number $N_p(E_\gamma, \theta_p, \phi)$ of true proton events by subtracting the accidental background.

Since the present measurements were carried out simultaneously at all photon energies and reaction angles the values for the polarization-independent part of the differential cross section and the azimuthal cross-section asymmetry may be obtained by the following equations [see eqs. (4) and (5)];

$$\frac{d\sigma_0}{d\Omega}(E_\gamma, \theta_p^{c.m.}) = \frac{C_{c.m.} C_d}{N_T N_\gamma} \frac{C_\parallel (N_p/\Delta\Omega)_\perp - C_\perp (N_p/\Delta\Omega)_\parallel}{C_\parallel - C_\perp}, \tag{6}$$

$$\Sigma(E_\gamma, \theta_p^{c.m.}) = \frac{1}{P} \frac{(N_p/\Delta\Omega)_\parallel - (N_p/\Delta\Omega)_\perp}{C_\parallel (N_p/\Delta\Omega)_\perp - C_\perp (N_p/\Delta\Omega)_\parallel}, \tag{7}$$

where $C_{c.m.}$ transforms the cross section to the center-of-mass system, $C_d = 1.117 \pm 0.003$ is the correction factor for the dead time of the acquisition system and $\Delta\Omega_{\parallel,\perp}$ are the effective solid angles considering the unavoidable asymmetric intensity distribution of the polarized tagged photons. The geometry factors $C_{\parallel,\perp}(E_\gamma, \theta_p)$ are averages of the $\cos 2\phi$ term over the finite size of the proton detectors; the absolute values of $C_{\parallel,\perp}$ are close to unity. The number of target nuclei N_T is given in subsect. 2.2 and the number of tagged photons N_γ and the degree of linear polarization P are listed in table 1. Twelve tagging detectors covering the energy range from 52 to 93 MeV were combined into four groups, the average photon energy (energy spread) of which are $E_\gamma = 54$ MeV (±3%), 60 MeV (±5%), 68 MeV (±5%) and 88 MeV (±5%).

4. Results and discussion

The present data for the polarization-independent part of the differential cross section $d\sigma_0/d\Omega$ and the azimuthal cross-section asymmetry Σ are presented in table 2 as a function of the photon energy in the laboratory system and the proton center-of-mass reaction angle. Also shown are the values for the corresponding polarization-dependent part of the differential cross section $d\sigma_1/d\Omega$. The uncertainties given in table 2 stem from the statistical error on the number of protons N_p, and - with the exception of Σ - from the statistical error on the number of tagged photons N_γ.

Systematic errors are caused by the uncertainties (quoted in parentheses) in the number N_T of target nuclei (±2.5%), in the knowledge of the degree of linear polarization P (±2%), in the solid angle $\Delta\Omega$ of the proton detectors (±1%) or the azimuthal asymmetry Σ_{app} of the apparatus (±0.007) and in the correction factor C_d for the dead time (±0.3%). Assuming $N_{p\parallel} \simeq N_{p\perp}$, $C_\parallel \simeq -C_\perp \simeq 1$ and $\Sigma_{app} \ll 1$ the systematic errors can be estimated using the following relations,

$$\frac{\Delta(d\sigma_0/d\Omega)_{syst}}{d\sigma_0/d\Omega} \simeq \sqrt{\left(\frac{\Delta N_T}{N_T}\right)^2 + \frac{1}{2}\left(\frac{\Delta(\Delta\Omega)}{\Delta\Omega}\right)^2}, \tag{8}$$

TABLE 2

Experimental values for the polarization-independent part of the differential cross section $d\sigma_0/d\Omega(E_\gamma, \theta_p^{c.m.})$ in μb/sr, for the azimuthal cross-section asymmetry $\Sigma(E_\gamma, \theta_p^{c.m.})$ and for the corresponding polarization-dependent part of the differential cross section $d\sigma_1/d\Omega(E_\gamma, \theta_p^{c.m.})$ in μb/sr. Only statistical errors are shown.

E_γ (MeV)	$\theta_p^{c.m.}$	$d\sigma_0/d\Omega$	Σ	$d\sigma_1/d\Omega$
54	46.6°	14.2 ± 0.5	0.50 ± 0.08	7.1 ± 1.1
	67.9°	15.6 ± 0.5	0.57 ± 0.06	9.0 ± 1.0
	88.2°	14.5 ± 0.5	0.63 ± 0.07	9.2 ± 1.1
	108.2°	13.0 ± 0.6	0.46 ± 0.09	6.0 ± 1.2
	127.1°	8.4 ± 0.5	0.42 ± 0.12	3.5 ± 1.0
	145.1°	6.4 ± 0.5	0.20 ± 0.16	1.3 ± 1.0
	162.6°	4.6 ± 0.4	0.00 ± 0.20	0.0 ± 0.9
60	46.9°	10.9 ± 0.5	0.41 ± 0.10	4.5 ± 1.1
	68.2°	11.7 ± 0.4	0.44 ± 0.07	5.1 ± 0.9
	88.6°	12.1 ± 0.4	0.45 ± 0.07	5.4 ± 0.9
	108.7°	9.7 ± 0.4	0.44 ± 0.09	4.3 ± 0.9
	127.4°	6.9 ± 0.4	0.20 ± 0.12	1.4 ± 0.8
	145.5°	6.0 ± 0.4	0.21 ± 0.14	1.2 ± 0.8
	162.7°	4.5 ± 0.4	0.19 ± 0.20	0.9 ± 0.9
68	47.6°	9.6 ± 0.6	0.35 ± 0.14	3.4 ± 1.4
	69.1°	11.6 ± 0.4	0.45 ± 0.08	5.2 ± 0.9
	89.4°	10.2 ± 0.4	0.31 ± 0.08	3.2 ± 0.9
	109.5°	8.6 ± 0.4	0.18 ± 0.10	1.6 ± 0.8
	128.2°	5.9 ± 0.3	0.17 ± 0.12	1.0 ± 0.7
	145.9°	4.5 ± 0.3	0.14 ± 0.13	0.6 ± 0.6
	163.0°	4.7 ± 0.3	0.10 ± 0.16	0.5 ± 0.8
88	71.0°	8.7 ± 0.5	0.16 ± 0.14	1.4 ± 1.2
	91.3°	6.8 ± 0.3	0.27 ± 0.11	1.9 ± 0.7
	111.3°	6.6 ± 0.3	0.21 ± 0.13	1.4 ± 0.8
	129.9°	4.5 ± 0.3	0.07 ± 0.14	0.3 ± 0.6
	147.4°	4.1 ± 0.2	0.02 ± 0.13	0.1 ± 0.5
	163.9°	4.2 ± 0.2	0.00 ± 0.17	0.0 ± 0.7

$$\Delta\Sigma_{syst} \simeq \sqrt{\left(\Sigma\frac{\Delta P}{P}\right)^2 + \left(\frac{\Delta\Sigma_{app}}{P}\right)^2}, \tag{9}$$

$$\Delta\left(\frac{d\sigma_1}{d\Omega}\right)_{syst} \simeq \sqrt{\left(\frac{d\sigma_1}{d\Omega}\right)^2\left[\left(\frac{\Delta P}{P}\right)^2 + \left(\frac{\Delta N_T}{N_T}\right)^2\right] + 2\left(\frac{d\sigma_0}{d\Omega}\right)^2\left(\frac{\Delta(\Delta\Omega)}{\Delta\Omega}\right)^2}. \tag{10}$$

Thus the relative systematic error for $d\sigma_0/d\Omega$ is estimated to be ±3%. For Σ a systematic error of about ±0.02 is obtained. The systematic error for $d\sigma_1/d\Omega$ varies significantly with θ_p and E_γ, i.e. between ±0.06 μb/sr and ±0.36 μb/sr according to eq. (10).

In the following, the present data are compared with earlier measurements and with the results of a recent theoretical treatment [16]). The predictions are calculated

in the framework of conventional non-relativistic nuclear theory using a realistic nucleon-nucleon potential and considering electromagnetic multipole transitions through $L = 4$. Meson-exchange current effects beyond the use of Siegert operators are treated explicitly. Internal nucleon excitations, so-called isobar degrees of freedom, are taken into account as wave-function components. Moreover, relativistic corrections to the nuclear current, which are dominated by the relativistic spin-orbit current, are included. Relativistic corrections in the wave functions are omitted. The predictions are shown for both the Paris and the r-space version of the Bonn potential.

The present data for $\Sigma(\theta_p^{c.m.})$ at $E_\gamma = 54$, 60, 68 and 88 MeV are shown in fig. 5. Within the statistical errors they on the whole agree with the results of the earlier measurements and with the theoretical predictions. Obviously there is no agreement with the point of Del Bianco *et al.*[8]) at 54 MeV and with the one of Ganenko *et al.*[12]) at 60 MeV. The points of Barannik *et al.*[9]) and Vnukov *et al.*[11]), both of which have extremely small statistical errors, tend to lower values than the present

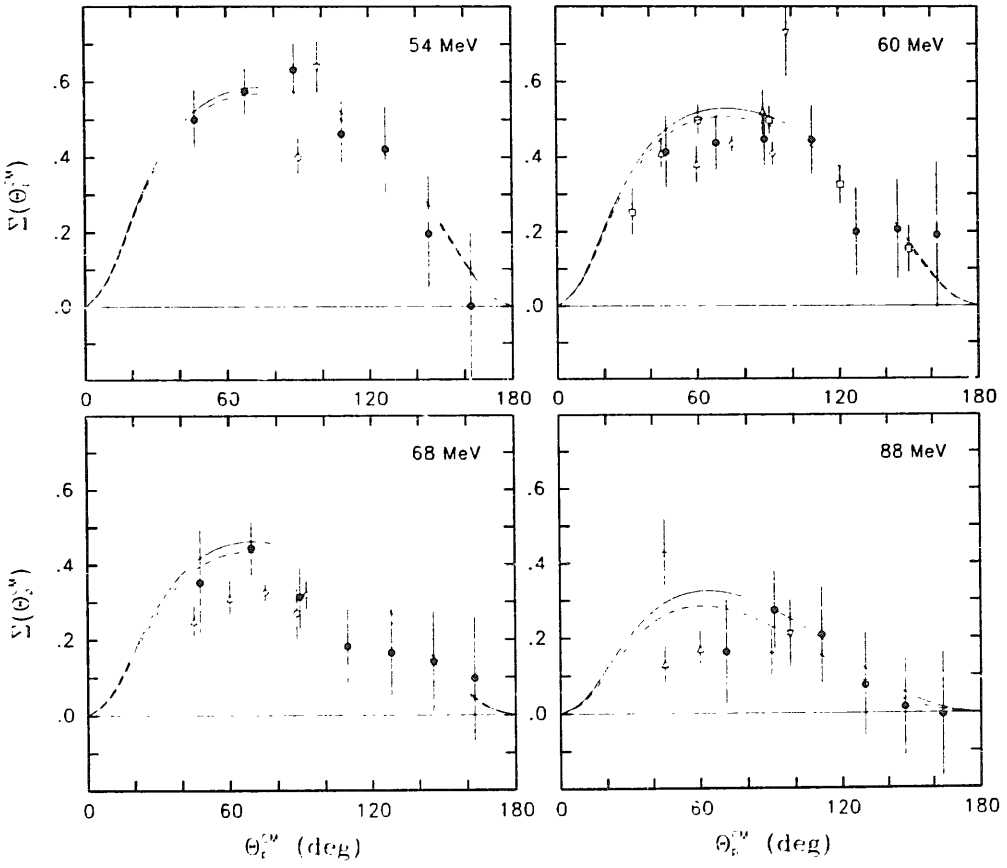

Fig. 5. Azimuthal cross-section asymmetry $\Sigma(\theta_p^{c.m.})$ as a function of the proton center-of-mass angle at $E_\gamma = 54$, 60, 68 and 88 MeV. The present data (●) are compared with the results of earlier measurements: ref.[7]) (+); ref.[8]) (○); ref.[9]) (◇); ref.[10]) (□); ref.[11]) (△) and ref.[12]) (▽). Only statistical errors are quoted except for ref.[11]), where systematic errors are included. For comparison, theoretical curves[16]) calculated for the Paris (dashed line) and the Bonn (solid line) potential are shown.

data and the data of De Pascale *et al.* [10]). Systematic differences between the data can be emphasized by averaging - regardless of energy resolution - over the whole range from 54 to 88 MeV separately for each experiment. The result is shown in fig. 6, where the statistically weighted mean differences between the data, Σ_{exp}, and the prediction, Σ_{theo}, are plotted as a function of the reaction angle. The thin lines represent the systematic error $\Delta\Sigma_{syst}$ for the present data. According to fig. 6 there is a good agreement between the present data and the data from ref. [10]), where measurements were made with an almost completely polarized photon beam from Compton backscattering of laser light. However, the data from refs. [8,9,11]), the latter two of which were measured with coherent bremsstrahlung, are systematically lower and the data from ref. [12]) systematically higher than the present data. The systematic errors quoted for the data from refs. [8,11]) cannot explain these discrepancies. In refs. [9,12]) systematic errors are not given at all. Furthermore, fig. 6 shows - at least on the average - a good agreement between the results of the present experiment and the prediction using the Paris potential. In the case of the Bonn potential, which leads to a stronger azimuthal asymmetry, the agreement is not as good.

The present results for $d\sigma_0/d\Omega(\theta_p^{c.m.})$, which represent here the first absolute measurements using tagged photons, are shown in fig. 7 together with the results

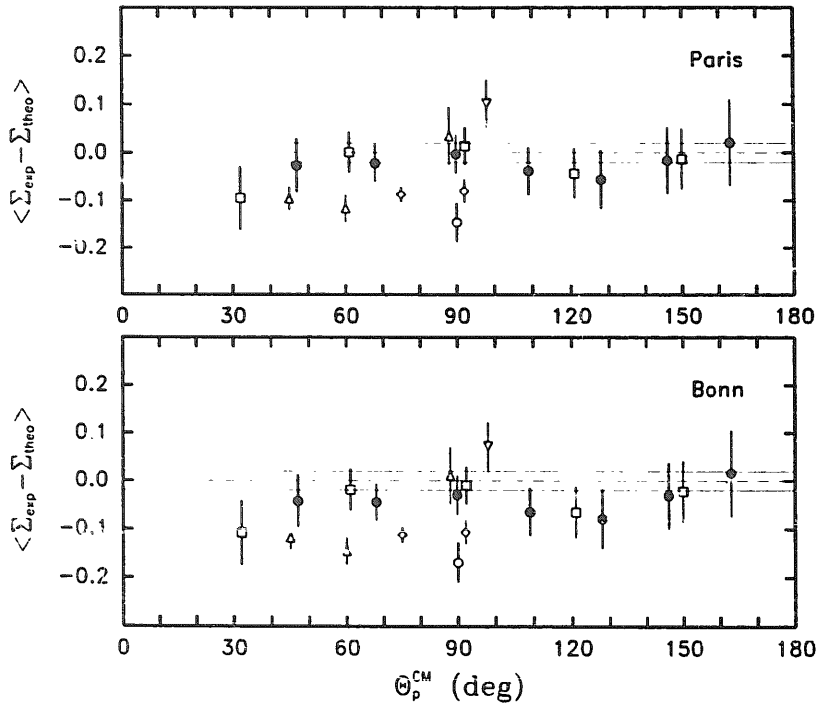

Fig. 6. Difference between experimental and theoretical azimuthal cross-section asymmetry, $\Sigma_{exp} - \Sigma_{theo}$, averaged separately for each experiment over the whole photon-energy range from 54 to 88 MeV as a function of the proton center-of-mass angle. The theoretical asymmetries [16]) applied for the procedure are based on the Paris and the Bonn potential, respectively. All symbols have the same meaning as in fig. 5. The thin lines represent the systematic error for the present data. See text.

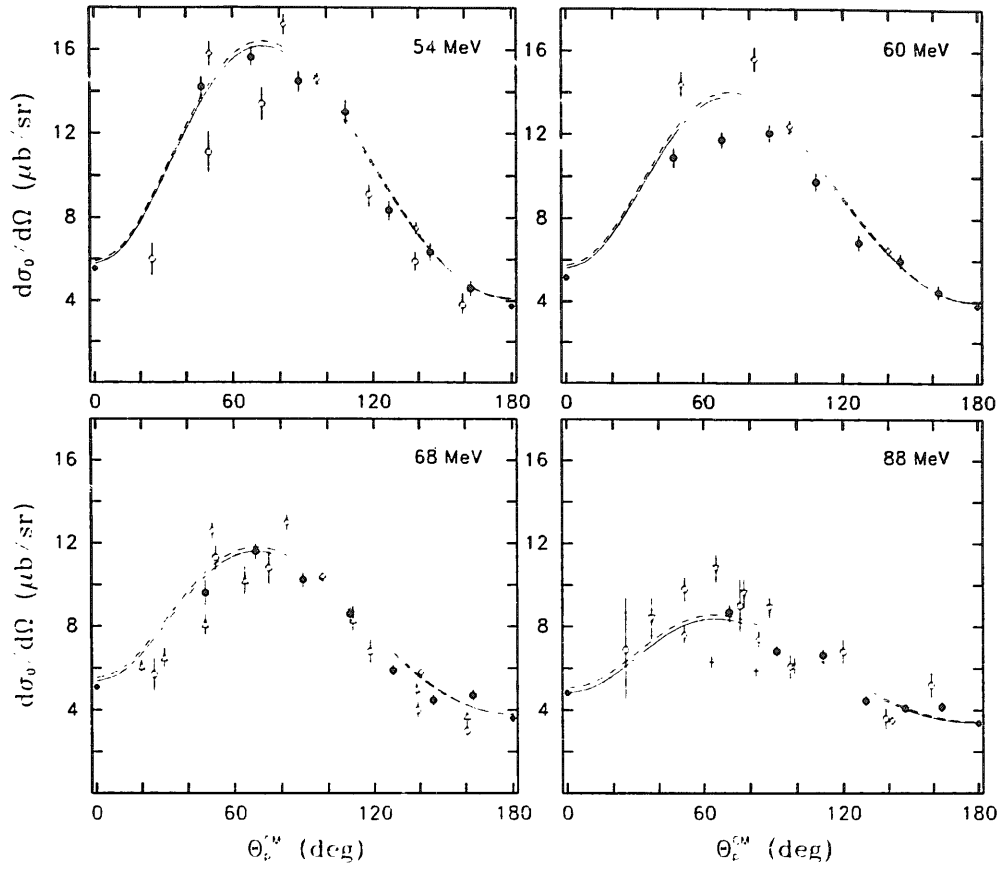

Fig. 7. Differential cross section $d\sigma_0/d\Omega$ for an unpolarized photon beam in the center-of-mass frame as a function of the proton angle at $E_\gamma = 54$, 60, 68 and 88 MeV. The present data (●) are compared with the results of earlier absolute measurements of the angular distribution: ref. [2]) (△); ref. [3]) (+); ref. [4]) (○); ref. [5]) (◇) and ref. [6]) (▽). Included are also the recent data from refs. [17,18]) (◆). Only statistical errors are shown. For comparison, theoretical curves [16]) calculated for the Paris (dashed line) and the Bonn (solid line) potential are shown.

of earlier experiments [2-6]). Also presented are the recently measured forward and backward differential cross sections of Zieger *et al.* [17,18]), the systematic error of which compares to the one of the present data. The wide band of absolute cross sections from earlier experiments, all of which were performed with continuous bremsstrahlung, may be attributed to the lack of an accurate evaluation of the incoming photon flux [19]). At $E_\gamma = 54$, 68 and 88 MeV the present data are located approximately in the center of this band and agree best with the theoretical prediction. At 60 MeV and backward angles there is still agreement with the prediction. However, at medium angles, especially at $\theta_p^{c.m.} = 70°$, the present data points are significantly lower than the predicted values. There is also no agreement with the only other absolute measurement [5]). The reason for the decrease of the present medium angle cross sections at 60 MeV is not known; however, it should be emphasized that due to the method applied here, a systematic error has to show up equally through all photon energies, and that is not the case.

The polarization-independent and dependent parts of the differential cross section, eq. (1), can be expanded in terms containing information about the electromagnetic multipole transitions involved. Including multipole distributions up to dipole-octupole interferences one has (here $\theta = \theta_p^{c.m.}$)

$$\frac{d\sigma_0}{d\Omega}(\theta) = a + b\sin^2\theta + c\cos\theta + d\sin^2\theta\cos\theta + e\sin^2\theta\cos^2\theta, \tag{11}$$

$$\frac{d\sigma_1}{d\Omega}(\theta) = f\sin^2\theta + g\sin^2\theta\cos\theta + h\sin^2\theta\cos^2\theta, \tag{12}$$

where $a, \ldots, h$ are energy-dependent coefficients. In the energy range considered here the photodisintegration of the deuteron is dominated by electric dipole transitions. Of course, the magnetic and electric quadrupole transitions also contribute significantly to the differential cross section. The isotropic term, a, and the coefficients b and f are mainly affected by pure E1 and M2 transitions. The coefficient c contains the E1-M1 and E1-E2 interference amplitudes. The E1-E2 interferences dominate the coefficients d and g, whereas pure E2 transitions enter the coefficients e and h.

The coefficients b, e, f and h are different from the corresponding coefficients of the expansion found in ref. [15]). There, the $\sin^2\theta\cos^2\theta$ terms from eqs. (11) and (12) have been dismantled and combined with the $\sin^2\theta$ terms, whereby the pure E2 transitions are mixed into b and f.

Alternatively, the differential cross section may be expanded in terms of Legendre polynomials, P_J, and associated Legendre functions, P_J^m,

$$\frac{d\sigma_0}{d\Omega}(\theta) = \sum_{J=0}^{4} A_J P_J(\cos\theta), \tag{13}$$

$$\frac{d\sigma_1}{d\Omega}(\theta) = \sum_{J=2}^{4} B_J P_J^2(\cos\theta), \tag{14}$$

where A_J and B_J are the energy-dependent coefficients. They are more transparently related to the multipole transitions involved, because of the simplicity of the expressions connecting A_J and B_J with the reduced transition matrix elements [20]). The total cross section is directly related to A_0, which of course contains only pure electric and magnetic transitions. A_1 is affected by E1-E2 and E1-M1 interferences. In the case of A_2 and B_2 the most significant contributions stem from pure E1 and M2 transitions. Each of the coefficients A_3, A_4, B_3 and B_4 is directly connected with d, e, g and h, respectively. The relationship between the two sets of expansion coefficients is given by

$$\begin{aligned}
A_0 &= a + \tfrac{2}{3}b + \tfrac{2}{15}e, & A_1 &= c + \tfrac{2}{5}d,\\
A_2 &= -\tfrac{2}{3}b + \tfrac{2}{21}e, & A_3 &= -\tfrac{2}{5}d,\\
A_4 &= -\tfrac{8}{35}e, & B_2 &= \tfrac{1}{3}f + \tfrac{1}{21}h,\\
B_3 &= \tfrac{1}{15}g, & B_4 &= \tfrac{2}{105}h.
\end{aligned} \tag{15}$$

In order to deduce the two sets of expansion coefficients a standard least-squares fit procedure was applied to the present data combined with the recently measured forward and backward differential cross sections from refs. [17,18]), which are the most accurate data available at the extreme angles. Only statistical errors are used in the fit procedure. The deduced values for $a, \ldots, h$ and $A_0, \ldots, B_4$ are shown in figs. 8 and 9 as a function of the photon energy. The error bars are derived from the least-squares fit procedure. Also shown are the corresponding predictions of the refined calculation [16]) evaluated with the Bonn and the Paris potential, and for comparison the results of a classical calculation (Bonn potential) that, in accordance with ref. [15]), omits contributions due to explicit meson-exchange currents, isobar configurations and relativistic effects.

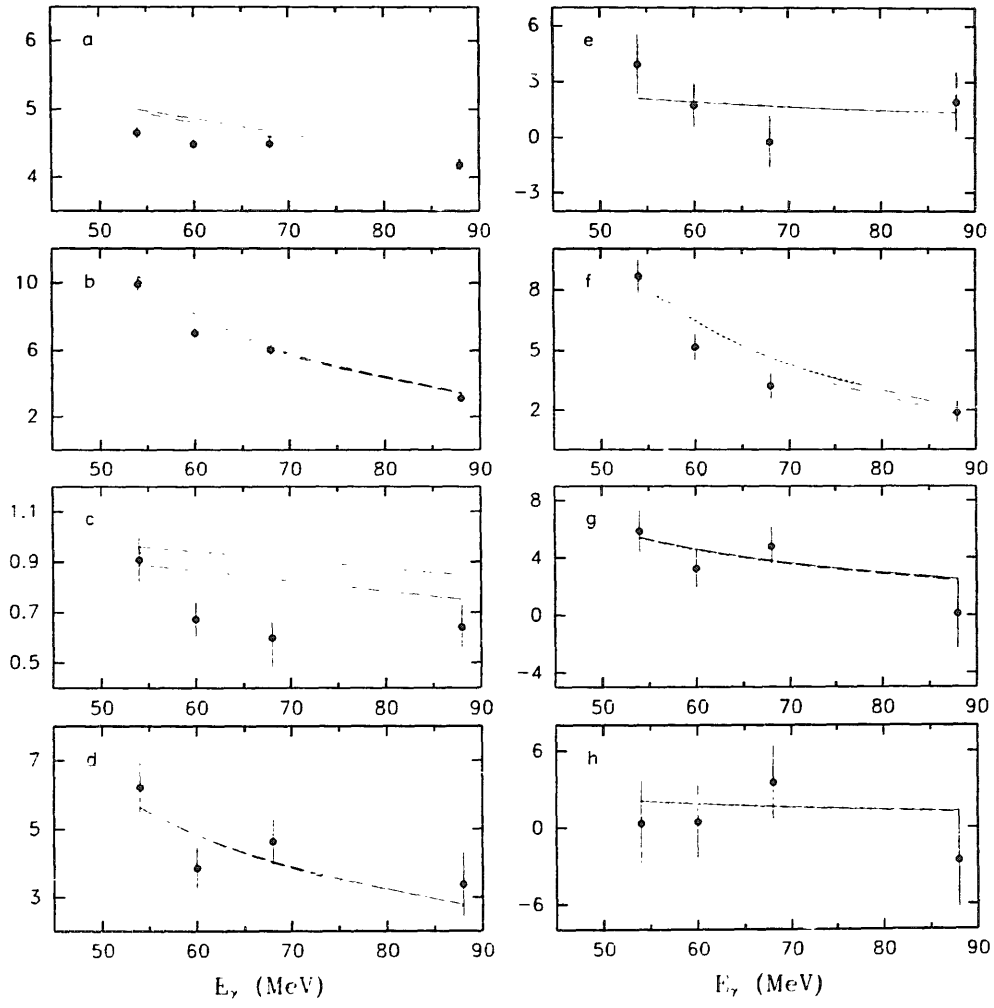

Fig. 8. Coefficients $a, \ldots, h$ of the expansion for the differential cross section given by eqs. (11) and (12) as a function of the photon energy. The error bars stem from the errors derived from the least-squares fit procedure applied to the present data combined with the forward and backward differential cross sections from refs. [17,18]). Also shown are the theoretical curves [16]) for the Bonn (solid line) and the Paris potential (dashed line) and for comparison the results of the classical calculation (Bonn potential, dotted line). The values are given in μb/sr.

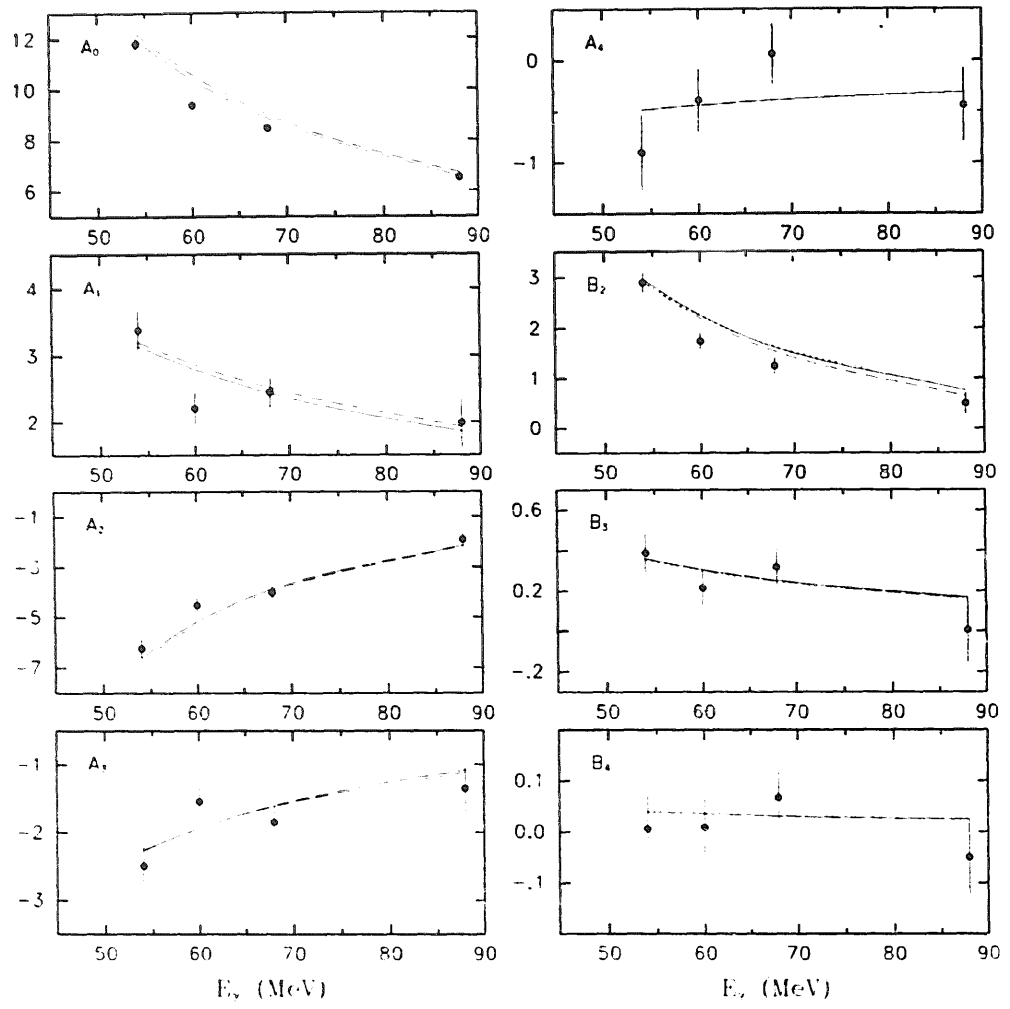

Fig. 9. Coefficients $A_0, \ldots, B_4$ of the Legendre expansion for the differential cross section given by eqs. (13) and (14) as a function of the photon energy. The error bars stem from the errors derived from the least-squares fit procedure applied to the present data combined with the forward and backward differential cross sections from refs. [17,18]). Also shown are the theoretical curves [16]) for the Bonn (solid line) and the Paris potential (dashed line) and for comparison the results of the classical calculation (Bonn potential, dotted line). The values are given in μb/sr.

The classical calculation is not able to reproduce the experimental values for the coefficients *a*, *b*, *c* and *f*. Compared with the quoted errors, the classical and the refined calculation result in similar predictions for *d*, *e*, *g* and *h*, both calculations agree with the experimental values. Adding the abovementioned corrections to the classical calculation leads to a substantial improvement concerning the coefficients *a* and *b*. The strong reduction of the isotropic term, *a*, mainly reflects the influence of relativistic effects [21]). The dominant contribution arises from the relativistic spin-orbit current, which preferably effects E1 transitions [16]). However, at the lower photon energies the refined values for *a* are still too high compared with the experimental results. Changes in the course of *b* are equally due to the inclusion of subnuclear degrees of freedom and relativistic effects. The refined curve agrees

TABLE 3

Coefficients of the expansion for the differential cross section given by eqs. (11) and (12) as a function of the photon energy. The errors stem from the errors derived from the least-squares fit procedure applied to the present data combined with the forward and backward differential cross sections from refs. [17,18]). The values are given in μb/sr.

E_γ (MeV)	54	60	68	88
a	4.7±0.1	4.5±0.1	4.5±0.1	4.2±0.1
b	9.9±0.4	7.0±0.3	6.0±0.3	3.1±0.2
c	0.9±0.1	0.7±0.1	0.6±0.1	0.6±0.1
d	6.2±0.7	3.8±0.6	4.6±0.7	3.4±0.9
e	3.9±1.6	1.7±1.2	−0.2±1.4	1.9±1.6
f	8.7±0.8	5.2±0.7	3.2±0.6	1.9±0.6
g	5.8±1.5	3.2±1.3	4.8±1.4	0.1±2.4
h	0.3±3.4	0.5±2.9	3.5±2.9	−2.6±4.0

with the experimental results except at 60 MeV, where the experimental value is significantly lower than the prediction. Differences are also to be seen in the case of c and f, but taking into account the systematic uncertainties of the data no definite conclusions can be drawn here. The Paris potential gives a slightly better agreement for the coefficient f, which describes the polarization-dependent part of the cross section at $\theta_p^{c.m.} = 90°$, whereas the Bonn potential, which leads to a weaker D-state admixture, results in a better description of a, b and c.

The estimated values for the total cross section, $\sigma_{tot} = 4\pi A_0$, agree within the statistical and systematic uncertainties with the theoretical calculations using the Bonn potential except - as was to be expected from the discussion of the differential

TABLE 4

Coefficients of the Legendre expansion for the differential cross section given by eqs. (13) and (14) as a function of the photon energy. The errors stem from the errors derived from the least-squares fit procedure applied to the present data combined with the forward and backward differential cross sections from refs. [17,18]). The values are given in μb/sr.

E_γ (MeV)	54	60	68	88
A_0	11.8±0.2	9.4±0.2	8.5±0.2	6.5±0.2
A_1	3.4±0.3	2.2±0.2	2.5±0.2	2.0±0.4
A_2	−6.2±0.4	−4.5±0.3	−4.0±0.3	−1.9±0.2
A_3	−2.5±0.3	−1.5±0.2	−1.9±0.3	−1.4±0.4
A_4	−0.9±0.4	−0.4±0.3	0.1±0.3	−0.4±0.4
B_2	2.9±0.2	1.7±0.2	1.2±0.2	0.5±0.2
$B_3 \times 10$	3.9±1.0	2.2±0.9	3.2±0.9	0.0±1.6
$B_4 \times 100$	0.6±6.5	0.9±5.6	6.7±5.5	−5.0±7.5

cross section - the point at 60 MeV, which is significantly lower than the prediction (see fig. 9). This effect is not to be seen in the azimuthal cross-section asymmetry Σ, since it is canceled out by the fact that the discrepancy also occurs in the polarization-dependent part of the differential cross section (see B_2 in fig. 9).

A list of all coefficients obtained by the least-squares fit procedure is given in tables 3 and 4.

5. Summary and conclusion

A quasi-monochromatic linearly polarized photon beam was used to simultaneously measure both the angular distribution of the azimuthal cross-section asymmetry and the polarization-independent part of the differential cross section in the photodisintegration of the deuteron at 54, 60, 68 and 88 MeV.

The photon beam was produced by tagging off-axis bremsstrahlung. The degree of polarization is considerably enhanced by means of a kinematic selection of the post-bremsstrahlung electrons. The photo-proton detectors are placed around a liquid-deuterium target at seven reaction angles both parallel and perpendicular to the polarization plane. Because of the high performance of the experimental setup the systematic errors in the data were kept extremely low.

The present data are compared with the results of other authors and with a recent theoretical treatment [16]), which considers subnuclear degrees of freedom as well as relativistic corrections to the nuclear current.

In the case of the azimuthal cross-section asymmetry the comparison shows that most of the asymmetries from refs. [9,11,12]) measured with coherent bremsstrahlung are distinctly different from the present data, whereas the result from ref. [10]) measured with an almost completely polarized photon beam from Compton backscattering of laser light is in agreement with the present data at that energy. The theory gives a satisfactory description of the present data.

The present data for the polarization-independent part of the differential cross section, which represent here the first absolute measurements using tagged photons, are located approximately half way between the widely scattered values from earlier experiments [2-6]). At 54, 68 and 88 MeV the present data agree best with the theoretical prediction. At 60 MeV and medium angles, especially at 70°, the points are significantly lower than the prediction.

A least-squares fit procedure was applied to the present data combined with the recently measured forward and backward differential cross sections from refs. [17,18]), in order to deduce the coefficients $a, \ldots, h$ as well as $A_0, \ldots, B_4$, the coefficients of the equivalent Legendre expansion for the differential cross section. The relationship between the two sets of expansion coefficients is given. The deduced coefficients demonstrate that the calculation without taking into account meson-exchange currents, isobar degrees of freedom and relativistic corrections is not able to describe all the experimental data, whereas the inclusion of these effects leads to an improved

description of the experimental results. However, significant differences are still to be seen in the coefficients a and b or A_0 and A_2, respectively.

As a concluding comment we can say that the theory of the photodisintegration of the deuteron extended beyond the classical non-relativistic treatment by the inclusion of subnuclear degrees of freedom and relativistic effects leads in general to a reasonable description not only of the present absolute data for the polarization-independent cross section but also for the azimuthal cross-section asymmetry. However, the distinct discrepancy seen at 60 MeV concerning both the polarization-independent and dependent part of the differential cross section needs to be clarified. New precise measurements and refined or extended calculations would be helpful in clarifying this discrepancy.

We wish to thank K.-H. Musshoff for his valuable technical assistance throughout the realization of the experiment. We are indepted to Dr. K.-H. Kaiser and the MAMI crew for the excellent operation of the accelerator. We thank Dr. A. Zieger for providing us in advance with the forward/backward cross sections. We would like to express our grateful acknowledgement to Professor H. Arenhövel, Dr. K.-M. Schmitt and P.-T. Wilhelm for discussions and making available the results of their calculations pertinent to our photon energies.

References

1) H. Arenhövel and M. Sanzone, Photodisintegration of the deuteron, Few-Body Systems, Suppl. 3 (Springer, Berlin, 1991)
2) L. Allen Jr., Phys. Rev. **98** (1955) 705
3) J.C. Keck and A.V. Tollestrup, Phys. Rev. **101** (1956) 360
4) I.A. Aleksandrov, N.B. Delone, L.I. Slovokhotov, G.A. Sokol and L.N. Shtarkov, Zh. Eksp. Teor. Fiz. **33** (1957) 614 [Sov. Phys. JETP **33** (1958) 472]
5) J.A. Galey, Phys. Rev. **117** (1960) 763
6) P. Dougan, V. Ramsay and W. Stiefler, Z. Phys. **A280** (1977) 341
7) F.F. Liu, Phys. Rev. **138** (1965) B1443
8) W. Del Bianco, L. Federici, G. Giordano, G. Matone, G. Pasquariello, P.G. Picozza, R. Caloi, L. Casano, M.P. De Pascale, L. Ingrosso, M. Mattioli, E. Poldi, C. Schaerf, P. Pelfer, D. Prosperi, S. Frullani, B. Girolami and H. Jeremie, Phys. Rev. Lett. **47** (1981) 1118
9) V.P. Barannik, V.G. Gorbenko, V.A. Gushchin, Yu.V. Zhebrovskiĭ, L.Ya. Kolesnikov, Yu.V. Kulish, A.L. Rubashkin and P.V. Sorokin, Yad. Fiz. **38** (1983) 1108 [Sov. J. Nucl. Phys. **38** (1983) 667]
10) M.P. De Pascale, G. Giordano, G. Matone, D. Babusci, R. Bernabei, O.M. Bilaniuk, L. Casano, S. d'Angelo, M. Mattioli, P. Picozza, D. Prosperi, C. Schaerf, S. Frullani and B. Girolami, Phys. Rev. **C32** (1985) 1830
11) I.E. Vnukov, M.N. Gushtan, I.V. Glavanakov, B.N. Kalinin, Yu.F. Krechetov, A.P. Potylitsyn, G.A. Saruev, V.N. Stibunov, A.N. Tabachenko, Pis'ma Zh. Eksp. Teor. Fiz. **43** (1986) 510 [JETP Lett. **43** (1986) 659];
I.E. Vnukov, I.V. Glavanakov, Yu.F. Krechetov, A.P. Potylitsyn, G.A. Saruev, V.N. Stibunov and A.N. Tabachenko, Yad. Fiz. **47** (1988) 913 [Sov. J. Nucl. Phys. **47** (1988) 581]
12) V.B. Ganenko, V.A. Gushchin, Yu.V. Zhebrovskiĭ, L.Ya. Kolesnikov, A.L. Rubashkin and P.V. Sorokin, Pis'ma Zh. Eksp. Teor. Fiz. **46** (1987) 216 [JETP Lett. **46** (1987) 272]
13) H. Hermighaus, B. Dreher, H. Euteneuer, K.-H. Kaiser, M. Kelliher, R. Klein, H.J. Kreidel, M. Loch, U. Ludwig-Mertin, K. Merle, H. Schoeler, R. Schulze, P. Semmel and G. Stephan, IEEE Trans. Nucl. Sci. **30** (1983) 3274

14) K.-H. Krause, J. Sobolewski, D. Hauff, J.M. Henneberg, N. Wieloch-Laufenberg, J. Ahrens, H. Gimm, A. Zieger and B. Ziegler, Nucl. Instr. Meth. A310 (1991) 577
15) F. Partovi, Ann. of Phys. 27 (1964) 79
16) P. Wilhelm, W. Leidemann and H. Arenhövel, Few-Body Systems 3 (1988) 111; private communication
17) A. Zieger, A. De Graeve, D. Christmann, R. Van de Vyver and B. Ziegler, Phys. Lett. B285 (1992) 1
18) A. Zieger, A. De Graeve, D. Christmann, R. Van de Vyver, C. Van den Abcele and B. Ziegler, Phys. Lett. B287 (1992) 51
19) M. Sanzone, Proc. Int. School of Intermediate Energy Nuclear Physics, Verona, 1985, ed. R. Bergère, S. Costa and C. Schaerf (World Scientific, Singapore, 1986) p. 78
20) A. Cambi, B. Mosconi and P. Ricci, Phys. Rev. C26 (1982) 2358
21) A. Cambi, B. Mosconi and P. Ricci, Phys. Rev. Lett. 48 (1982) 462